

# High order generalized finite difference schemes with compact support for compressible flows

Xue-Li Li\*, Yu-XinRen\*

Corresponding author: ryx@mail.tsinghua.edu.cn

\* School of aerospace engineering, Tsinghua university, Beijing 100084, China

**Abstract:** In this paper we propose a new class of high order generalized finite difference schemes on a compact stencil. The variational method is used in the reconstruction procedure. A simple and efficient hybrid approach is proposed for constructing the upwind numerical flux derivatives on a compact stencil. The reconstruction and implicit time integration coupled iterative technique is used to improve the computational efficiency. A new flexible high order boundary treatment is presented in this paper. The WBAP limiter is used to suppress oscillations near discontinuities. Several numerical test cases are solved to validate the accuracy, efficiency, and shock capturing capability of the proposed high order schemes.

*Keywords:* High order compact schemes, Variational reconstruction, Boundary treatment, Shock capturing, WBAP limiter.

## 1 Introduction

Generalized finite difference (GFD) method represents a general class of numerical methods that can handle problems with complicated geometries. Compared with the unstructured finite volume method, this method uses only clouds of points to discretize the partial differential equations and there is no need to perform the spatially numerical integration. When the clouds of points are extracted from the existing grids, GFD method may be considered as the finite difference method based on the unstructured grids. When the clouds of points are independent to any kinds of grid structures, GFD method is a certain kind of meshless methods. In the latter case, GFD method may fall under many other names including meshless [1-6], meshfree [7, 8], gridfree [9, 10], gridless [11-15], LSFD-U [16, 17], and finite point [18-21] methods.

In the past two decades, extensive studies have been carried out in developing GFD or meshless methods for solving the compressible and incompressible flows. GFD method was firstly proposed by Chung [22]. Batina [1] developed an explicit gridless solver using a least-square curve fit on local cloud of points. Löhner et al. [19] used a linear polynomial to construct the flux distribution and adopted the method similar to one-dimensional MUSCL interpolation to compute the left and right states of the corresponding approximate Riemann solvers. Sridar and Balakrishnan [16] proposed an upwind least squares to construct the meshless schemes of specified order accuracy and used a linear fitting to approximate the spatial flux derivatives. Ding et al. [7] presented a 3rd order meshless scheme for incompressible flows and analyzed the error for derivatives. Shu et al. [23], Tota and Wang [8] used the radial basis functions to construct the flux derivatives. Katz and Jameson [2] used three approaches including Taylor series least-square, polynomial base least-square and radial base function methods to approximate spatial derivatives. Su and Yamaoto [5] analyzed some behaviors of the meshless methods with a linear fitting. Sundar and Yeo [6] presented a high order meshless

method with compact support for solving the incompressible flows. These methods are mainly first or second order in accuracy. While there have been some proposals for developing high order GFD schemes solving incompressible flows, very little work has been done on developing high order GFD schemes to compute compressible flows.

High order schemes are attractive for their significant potential to improve the spatial accuracy and to accelerate the rate of grid convergence compared to the traditional second order scheme. In our recent paper [Li, Ren, et al., 24], a general framework has been proposed for constructing high order GFD schemes for solving the inviscid compressible flows. The reconstruction and flux evaluation are two key ingredients in obtaining high order spatial accuracy. A large stencil is required in obtaining high order accuracy for the reconstruction and flux evaluation. The large stencil is a serious problem [25-26] for high order GFD schemes, which will reduce the computational efficiency especially in parallel computing and brings difficulties in the high order boundary treatment.

In the present work, a new GFD method is presented to circumvent the large stencil problem. This method can achieve arbitrarily high order accuracy on a highly compact stencil for both the reconstruction and flux evaluation. Firstly, a variational reconstruction is proposed based on the minimization of a cost function which is defined by the continuity of the solution and its derivatives. The solutions in the form of high order polynomials are recovered from this procedure by solving a system of linear equations. The similar procedure has been proposed for the high order finite volume methods in [28]. The present method, however, is based on the point-wise values of the solution instead of the cell averages for the finite volume methods. Secondly, a simple and efficient hybrid approach is proposed to construct the upwind numerical flux derivatives. Comparing with the derivative Riemann solver approach [29] which can also be used to compute the numerical flux derivatives, the present approach is several times more efficient.

The variational reconstruction method is implicit in nature and a large system of linear equations needs to be solved. When a direct solver is used, the computation is computationally expensive and the compactness of the reconstruction procedure is lost. The use of the iterative solvers can maintain the compactness of the solution procedure, which is still very expensive as the solution reaches full convergence. To improve the computational efficiency, the reconstruction and time integration coupled iterative technique proposed in [27] is used in the context of the GFD schemes. It should be noticed that it is required to use the implicit time stepping scheme when using this technique.

In our previous work [24], the high order boundary treatment consists of two steps, i.e., the extrapolation-correction step and the gradient reconstruction step. However, the stencils corresponding to these two steps are different and both could be very large. In the present paper, the extrapolation can also be carried out with the variational reconstruction technique. By the introduction of the boundary cost function, the extrapolation can be solved seamlessly together with the reconstruction of the non-boundary points. Furthermore, this extrapolation technique makes both the value of the extrapolated variable and its derivatives into one single step.

The remainder of this paper is organized as follows. The high order GFD schemes, the boundary treatment, and the WBAP limiter are described in the second section. Several numerical test cases are chosen in the third section to validate the performance of the proposed GFD schemes. Finally, conclusions are given in the last section.

## 2 High order compact GFD method

### 2.1 Governing equations

The two-dimensional unsteady compressible Euler equations are used as the governing equations and the conservation form can be expressed as

$$\frac{\partial \mathbf{U}}{\partial t} + \frac{\partial \mathbf{F}}{\partial x} + \frac{\partial \mathbf{G}}{\partial y} = \mathbf{0}, \quad (1)$$

where the conservative variables  $\mathbf{U}$  and the inviscid fluxes  $\mathbf{F}$ ,  $\mathbf{G}$  are given by

$$\mathbf{U} = \begin{bmatrix} \rho \\ \rho u \\ \rho v \\ E \end{bmatrix}, \quad \mathbf{F} = \begin{bmatrix} \rho u \\ \rho u^2 + p \\ \rho uv \\ u(E + p) \end{bmatrix}, \quad \mathbf{G} = \begin{bmatrix} \rho v \\ \rho uv \\ \rho v^2 + p \\ v(E + p) \end{bmatrix}.$$

Here,  $\rho$  is the density,  $u$  and  $v$  are the velocity components in  $x$  and  $y$  directions,  $p$  is the pressure, and  $E$  is the total energy per unit volume.

## 2.2 Basic framework of high order GFD schemes

Consider a local 2D cloud of scattered points surrounding a reference point  $i$  and two types of stencil points are defined, as shown in Fig. 1. The first stencil points are the support points (the dotted points) where the flow variables are stored. The second stencil points are the mid-points (the cross points) where the numerical fluxes are evaluated. The mid-points stand halfway between the reference point and the surrounding support points. These two stencil points provide the basic data structures of the high order accurate GFD schemes.

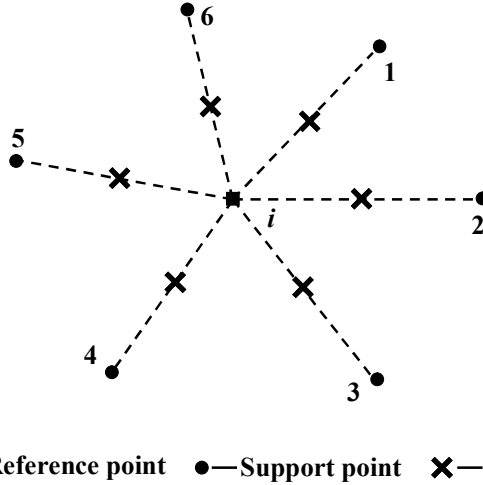


Fig. 1. Two types of stencils points defined in the local cloud of points.

Similarly to our recent work [24], the new GFD schemes also consist of three basic steps, i.e., the reconstruction, the flux evaluation, and the update step. The previous schemes are briefly reviewed before presenting the present work. Firstly, a piecewise polynomial is recovered from the point values on the reference point and its support points. Secondly, the numerical flux derivatives are computed in terms of the numerical fluxes on the mid-points. The numerical fluxes are computed using the high order interpolation with the reconstruction step and a certain Riemann solver or flux-splitting technique. Thirdly, the flow variables are updated with the time integration. In our pervious work, the number of support points is usually large since only the point values are used to construct the solution data and its derivatives. To circumvent the large stencil problem, a new high order GFD scheme is proposed on a highly compact support nodal set (stencil). The details of the solution procedure are described in the following steps.

### (1) Reconstruction step.

Given the numerical solutions at a certain time step, the distribution of the flow variables around the reference point  $i$  can be obtained using the reconstruction step. For simplicity, it is assumed that  $u(\mathbf{r})$  is a component of the conservative variables or the primitive variables. A piecewise polynomial of degree  $k$  is defined on the reference point  $i$  in the form

$$u_i(\mathbf{r}) = u_i + \sum_{l=1}^K u_i^l \phi_i^l(\mathbf{r}). \quad (2)$$

In Eq. (2),  $u_i^l$  are the unknown coefficients,  $\varphi_i^l(\mathbf{r})$  are the polynomial basis functions, and  $K$  is the number of unknown coefficients, i.e.,  $K = k(k+3)/2$  for the two-dimensional problems. In the present work, the polynomial basis functions  $\varphi_i^l(\mathbf{r})$  are defined as

$$\begin{aligned}\varphi_i^1(\mathbf{r}) &= \frac{x-x_i}{h_i}, \quad \varphi_i^2(\mathbf{r}) = \frac{y-y_i}{h_i}, \quad \varphi_i^3(\mathbf{r}) = \frac{(x-x_i)^2}{2h_i^2}, \\ \varphi_i^4(\mathbf{r}) &= \frac{(x-x_i)(y-y_i)}{h_i^2}, \quad \varphi_i^5(\mathbf{r}) = \frac{(y-y_i)^2}{2h_i^2}, \quad \dots,\end{aligned}\tag{3}$$

where  $(x_i, y_i)$  denotes the position of the reference point  $i$ , and  $h_i$  denotes the characteristic length scale of the reference point  $i$ .

In carrying out the reconstruction step, it is necessary to identify the stencil points. For simplicity, the stencil points are extracted from the existing grid topology using approaches similar to those of Katz and Jameson [1], Su et al. [5], Tota and Wang [8], and Munikrishna and Balakrishnan [17]. In the present work, a compact stencil  $S_i$  is used that only include the neighboring points sharing the common edges with the reference point, as shown in Fig. 2.

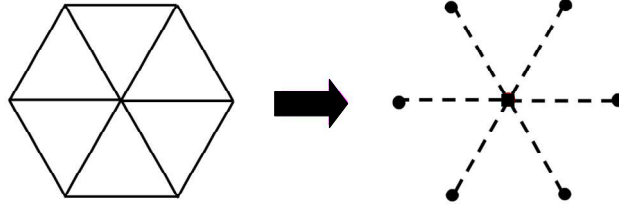


Fig. 2. Compact stencil extracted from the existing grid topology.

Based on the compact stencil  $S_i$ , the variational reconstruction is used in the present work. The variational reconstruction method represents a general class of reconstruction method [26]. The basic idea of the variational reconstruction is to compute the unknown coefficients by asking Eq. (2) to minimize a cost function using the direct variational approach. In the present work, the cost function at the reference point  $i$  can be defined as

$$\begin{aligned}J_i &= \sum_{j \in S_i} w_{ij} \left\{ \left( u_i(\mathbf{r}_{ij}) - u_j(\mathbf{r}_{ij}) \right)^2 + \Delta r_{ij}^2 \left[ \left( u_{i,x}(\mathbf{r}_{ij}) - u_{j,x}(\mathbf{r}_{ij}) \right)^2 \right. \right. \\ &\quad \left. \left. + \left( u_{i,y}(\mathbf{r}_{ij}) - u_{j,y}(\mathbf{r}_{ij}) \right)^2 \right] + \Delta r_{ij}^4 \left[ \left( u_{i,xx}(\mathbf{r}_{ij}) - u_{j,xx}(\mathbf{r}_{ij}) \right)^2 \right. \right. \\ &\quad \left. \left. + \left( u_{i,xy}(\mathbf{r}_{ij}) - u_{j,xy}(\mathbf{r}_{ij}) \right)^2 + \left( u_{i,yy}(\mathbf{r}_{ij}) - u_{j,yy}(\mathbf{r}_{ij}) \right)^2 \right] + \dots \right\},\end{aligned}\tag{4}$$

where  $\Delta r_{ij}$  denotes the distance of the mid-point  $ij$  from the reference point  $i$ , and  $w_{ij}$  is the weighted function given by

$$w_{ij} = \frac{1}{\Delta r_{ij}^Z}, \quad Z \geq 0.\tag{5}$$

In Eq. (4),  $\Delta r_{ij}^{2n}$  is used to balance the dimension of difference terms. The mid-point  $ij$  corresponding to the support point is  $j \in S_i$  located at

$$(x_{ij}, y_{ij}) = \left( \frac{x_i + x_j}{2}, \frac{y_i + y_j}{2} \right),$$

and the characteristic length scale of the reference point  $i$  in Eq. (3) can be defined by

$$h_i = \max_{j \in S_i} \Delta r_{ij} = \max_{j \in S_i} \sqrt{(x_{ij} - x_i)^2 + (y_{ij} - y_i)^2}. \quad (6)$$

The unknowns in Eq. (2) can be computed by minimizing the cost function  $J_i$  with unknown coefficients  $u_i^q$  in Eq. (2), i.e.,

$$\frac{\partial J_i}{\partial u_i^q} = 0, \quad q = 1, 2, \dots, K. \quad (7)$$

By substituting Eq. (2) into Eq. (8), a series of linear equations can be derived

$$\begin{aligned} & \sum_{l=1}^K u_i^l \sum_{j \in S_i} w_{ij} \left[ \varphi_i^l \varphi_i^q + \omega_1 \Delta r_{ij}^2 \left( \varphi_{i,x}^l \varphi_{i,x}^q + \varphi_{i,y}^l \varphi_{i,y}^q \right) + \omega_2 \Delta r_{ij}^4 \left( \varphi_{i,xx}^l \varphi_{i,xx}^q \right. \right. \\ & \left. \left. + \varphi_{i,xy}^l \varphi_{i,xy}^q + \varphi_{i,yy}^l \varphi_{i,yy}^q \right) + \dots \right] \\ & = \sum_{j \in S_i} w_{ij} \sum_{l=1}^K u_j^l \left[ \varphi_j^l \varphi_i^q + \omega_1 \Delta r_{ij}^2 \left( \varphi_{j,x}^l \varphi_{i,x}^q + \varphi_{j,y}^l \varphi_{i,y}^q \right) + \omega_2 \Delta r_{ij}^4 \left( \varphi_{j,xx}^l \varphi_{i,xx}^q \right. \right. \\ & \left. \left. + \varphi_{j,xy}^l \varphi_{i,xy}^q + \varphi_{j,yy}^l \varphi_{i,yy}^q \right) + \dots \right] + \sum_{j \in S_i} w_{ij} \varphi_i^q (u_j - u_i), \quad q = 1, 2, \dots, K. \end{aligned} \quad (8)$$

These equations can be written in matrix-vector form,

$$\mathbf{A}_{ii} \mathbf{u}_i = \sum_{j \in S_i} \mathbf{A}_{ij} \mathbf{u}_j + \mathbf{b}_i, \quad (9)$$

where

$$\begin{aligned} (u_i)_l &= u_i^l, \quad (b_i)_q = \sum_{j \in S_i} w_{ij} \varphi_i^q (u_j - u_i), \\ (a_{ii})_{ql} &= \sum_{j \in S_i} w_{ij} \left[ \varphi_i^q \varphi_i^l + \omega_1 \Delta r_{ij}^2 \left( \varphi_{i,x}^q \varphi_{i,x}^l + \varphi_{i,y}^q \varphi_{i,y}^l \right) + \omega_2 \Delta r_{ij}^4 \left( \varphi_{i,xx}^q \varphi_{i,xx}^l \right. \right. \\ & \left. \left. + \varphi_{i,xy}^q \varphi_{i,xy}^l + \varphi_{i,yy}^q \varphi_{i,yy}^l \right) + \dots \right], \\ (a_{ij})_{ql} &= w_{ij} \left[ \varphi_i^q \varphi_j^l + \omega_1 \Delta r_{ij}^2 \left( \varphi_{i,x}^q \varphi_{j,x}^l + \varphi_{i,y}^q \varphi_{j,y}^l \right) + \omega_2 \Delta r_{ij}^4 \left( \varphi_{i,xx}^q \varphi_{j,xx}^l \right. \right. \\ & \left. \left. + \varphi_{i,xy}^q \varphi_{j,xy}^l + \varphi_{i,yy}^q \varphi_{j,yy}^l \right) + \dots \right]. \end{aligned}$$

For all nodal points in the computational domain, the linear system in Eq. (9) can be assembled into a large linear system,

$$\mathbf{A} \mathbf{u} = \mathbf{b}, \quad (10)$$

where  $\mathbf{u} = \{\mathbf{u}_i\}$ ,  $\mathbf{b} = \{\mathbf{b}_i\}$ ,  $\mathbf{A} = \mathbf{D} - \mathbf{L} - \mathbf{U}$ ,  $\mathbf{D} = \{\mathbf{A}_{ii}\}$ ,  $\mathbf{L} = \{\mathbf{A}_{ij}, j < i\}$ , and  $\mathbf{R} = \{\mathbf{A}_{ij}, j > i\}$ .

The solution of Eq. (11) relies on all the nodal points in the computational domain. If a direct solver is used to solve Eq. (11), the computation is very expensive and the solution procedure is by no means compact. In the present work, the iterative solvers are used to solve the above equation to maintain the compactness of the solution procedure. There are several iterative solvers, such as the block Jacobi method, the block Gauss-Seidel method, and SOR method. In the present paper, the block Gauss-Seidel method is used, i.e.,

$$\mathbf{u}_i^{(m)} = \sum_{j \in S_i, j < i} \mathbf{A}_{ii}^{-1} \mathbf{A}_{ij} \mathbf{u}_j^{(m)} + \sum_{j \in S_i, j > i} \mathbf{A}_{ii}^{-1} \mathbf{A}_{ij} \mathbf{u}_j^{(m-1)} + \mathbf{A}_{ii}^{-1} \mathbf{b}_i, \quad (11)$$

where  $\mathbf{A}_{ii}^{-1}$  is inverse of the matrix  $\mathbf{A}_{ii}$  and  $m$  denotes the iterative step. The matrices  $\mathbf{A}_{ii}^{-1}$  and  $\mathbf{A}_{ii}^{-1} \mathbf{A}_{ij}$  are only geometry related, and can be computed only once and stored.

## (2) Flux evaluation step.

In this step, the spatial derivatives  $\mathbf{F}_x$  and  $\mathbf{G}_y$  at the reference point  $i$  will be computed. Assume that  $f$  is a component of the flux term  $\mathbf{F}$  or  $\mathbf{G}$ , which can be approximated by a degree  $k$

polynomial,

$$f_i(\mathbf{r}) = f_i + \sum_{l=1}^K f_i^l \varphi_i^l(\mathbf{r}) = f_i + f_i^1 \cdot \frac{\Delta x}{h_i} + f_i^2 \cdot \frac{\Delta y}{h_i} + (\text{H.O.T.})_i^f(\mathbf{r}), \quad (12)$$

where  $\Delta x = x - x_i$ ,  $\Delta y = y - y_i$ , and  $(\text{H.O.T.})_i^f(\mathbf{r})$  denotes the high order terms, i.e.,

$$(\text{H.O.T.})_i^f(\mathbf{r}) = f_i^2 \cdot \frac{\Delta y}{h_i} + f_i^3 \cdot \frac{\Delta x^2}{2h_i^2} + f_i^4 \cdot \frac{\Delta x \Delta y}{h_i^2} + f_i^5 \cdot \frac{\Delta y^2}{2h_i^2} + \dots \quad (13)$$

There are several possible approaches to compute  $\mathbf{F}_x$  and  $\mathbf{G}_y$ . The first and simplest approach is to derive Eq. (12) directly from the reconstruction polynomial  $u_i(\mathbf{r})$  obtained in the previous step. However, this approach does not provide any upwind mechanism and is deemed as unstable. The second approach is to firstly compute the mid-point flux using a certain upwind technique, and to use the mid-point flux to reconstruct Eq. (12). This is a traditional approach, and has been used in [16, 24]. The shortcoming of this approach is that it requires a large stencil since the number of known coefficients in Eq. (12) increases fast with the degree of the polynomial. Therefore, this approach may destroy the compactness of the present scheme. The third approach that may maintain the compactness of the scheme is to compute the fluxes of the dependent variables and their derivatives at the mid-points. If sufficient higher order derivatives can be computed, then the numerical fluxes can be evaluated on a compact stencil. The derivatives of the fluxes at the mid-points can be computed by solving the derivative Riemann solvers [29]. However, this approach is computationally expensive.

In the present work, a new simple and efficient approach is proposed for computing the numerical fluxes on a compact stencil. This approach can be considered as the hybridization of the first and second approaches. It is noted that the key to compute the spatial derivatives is the evaluation of  $f_i^1$  and  $f_i^2$  in Eq. (12). If the high order terms in Eq. (12) are directly derived from the reconstruction step, the number of the unknowns in Eq. (12) can be effectively reduced to 2. The compact stencil  $S_i$  that used in the reconstruction step is sufficient for the flux evaluation step. Similarly to the second approach, the flux evaluation is carried based on the mid-point  $ij$  to introduce the upwind mechanism. The details of the proposed hybrid approach are described in the following.

On every mid-point  $ij$ , there is the following interpolation relation,

$$f_i^1 \cdot \frac{\Delta x_{ij}}{h_i} + f_i^2 \cdot \frac{\Delta y_{ij}}{h_i} = \Delta f_{ij} - (\text{H.O.T.})_i^f(\mathbf{r}_{ij}), \quad j \in S_i, \quad (14)$$

where  $\Delta x_{ij} = x_{ij} - x_i$ ,  $\Delta y_{ij} = y_{ij} - y_i$ , and  $\Delta f_{ij} = f_{ij} - f_i$ . The numerical flux  $f_{ij}$  at the mid-point  $ij$  can be computed using a Riemann solver or flux splitting technique, and the high order term  $(\text{H.O.T.})_i^f(\mathbf{r}_{ij})$  can be derived from the reconstruction step. Further details will be given later in this section. After computing  $(\text{H.O.T.})_i^f(\mathbf{r}_{ij})$  and  $f_{ij}$ , the unknown terms in Eq. (14) can be solved by minimizing the following cost function,

$$J_{i,f} = \sum_{j \in S_i} w_{ij} \left[ \Delta f_{ij} - (\text{H.O.T.})_i^f(\mathbf{r}_{ij}) - \left( f_i^1 \cdot \frac{\Delta x_{ij}}{h_i} + f_i^2 \cdot \frac{\Delta y_{ij}}{h_i} \right) \right]^2, \quad (15)$$

where the weights  $w_{ij}$  are the same as those defined in Eq. (5). Once the coefficients are computed using the least-squares, the numerical flux derivatives at the reference point  $i$  can be obtained,

$$\left( \frac{\partial f}{\partial x} \right)_i = \frac{1}{h_i} \sum_{j \in S_i^k} \alpha_{ij} \left[ \Delta f_{ij} - (\text{H.O.T.})_i^f(\mathbf{r}_{ij}) \right], \quad (16)$$

$$\left( \frac{\partial f}{\partial y} \right)_i = \frac{1}{h_i} \sum_{j \in S_i^k} \beta_{ij} \left[ \Delta f_{ij} - (\text{H.O.T.})_i^f(\mathbf{r}_{ij}) \right], \quad (17)$$

where the coefficients  $(\alpha_{ij}, \beta_{ij})$  are only geometry related and can be calculated as

$$\alpha_{ij} = \frac{w_{ij} \frac{\Delta x_{ij}}{h_i} \sum_{k \in S_i} w_{ik} \frac{\Delta y_{ik}^2}{h_i^2} - w_{ij} \frac{\Delta y_{ij}}{h_i} \sum_{k \in S_i} w_{ik} \frac{\Delta x_{ik} \Delta y_{ik}}{h_i^2}}{\sum_{k \in S_i} w_{ik} \frac{\Delta x_{ik}^2}{h_i^2} \sum_{k \in S_i} w_{ik} \frac{\Delta y_{ik}^2}{h_i^2} - \left( \sum_{k \in S_i} w_{ik} \frac{\Delta x_{ik} \Delta y_{ik}}{h_i^2} \right)^2}, \quad (18)$$

$$\beta_{ij} = \frac{w_{ij} \frac{\Delta y_{ij}}{h_i} \sum_{k \in S_i} w_{ik} \frac{\Delta x_{ik}^2}{h_i^2} - w_{ij} \frac{\Delta x_{ij}}{h_i} \sum_{k \in S_i} w_{ik} \frac{\Delta x_{ik} \Delta y_{ik}}{h_i^2}}{\sum_{k \in S_i} w_{ik} \frac{\Delta x_{ik}^2}{h_i^2} \sum_{k \in S_i} w_{ik} \frac{\Delta y_{ik}^2}{h_i^2} - \left( \sum_{k \in S_i} w_{ik} \frac{\Delta x_{ik} \Delta y_{ik}}{h_i^2} \right)^2}. \quad (19)$$

Assume that the high order reconstruction polynomial in Eq. (2) has been recovered with variational reconstruction procedure. The left reconstruction state  $u_{ij}^L$  on the mid-points can then be computed, i.e.,

$$u_{ij}^L = u_i + u_i^1 \frac{\Delta x_{ij}}{h_i} + u_i^2 \frac{\Delta y_{ij}}{h_i} + (\text{H.O.T.})_i^u(\mathbf{r}_{ij}), \quad (20)$$

where  $\Delta x_{ij} = x_{ij} - x_i$ ,  $\Delta y_{ij} = y_{ij} - y_i$ , and  $(\text{H.O.T.})_i^u(\mathbf{r}_{ij})$  denotes the high order term in the reconstruction polynomial, i.e.,

$$(\text{H.O.T.})_i^u(\mathbf{r}_{ij}) = u_i^3 \frac{\Delta x_{ij}^2}{2h_i^2} + u_i^4 \frac{\Delta x_{ij} \Delta y_{ij}}{h_i^2} + u_i^5 \cdot \frac{\Delta y_{ij}^2}{2h_i^2} + \dots \quad (21)$$

The left flux state  $f_{ij}^L$  can be derived directly from Eq. (20), i.e.,

$$f_{ij}^L = f_i + \bar{f}_i^1 \frac{\Delta x_{ij}}{h_i} + \bar{f}_i^2 \frac{\Delta y_{ij}}{h_i} + (\text{H.O.T.})_i^{\bar{f}}(\mathbf{r}_{ij}), \quad (22)$$

where  $\bar{f}_i^l$  are derived coefficients from the reconstruction polynomial coefficients  $u_i^l$ , and  $(\text{H.O.T.})_i^{\bar{f}}(\mathbf{r}_{ij})$  is the derived high order terms, i.e.,

$$(\text{H.O.T.})_i^{\bar{f}}(\mathbf{r}_{ij}) = \bar{f}_i^3 \frac{\Delta x_{ij}^2}{2h_i^2} + \bar{f}_i^4 \frac{\Delta x_{ij} \Delta y_{ij}}{h_i^2} + \bar{f}_i^5 \cdot \frac{\Delta y_{ij}^2}{2h_i^2} + \dots \quad (23)$$

The derived high order terms  $(\text{H.O.T.})_i^{\bar{f}}(\mathbf{r}_{ij})$  in Eq. (22) is used for the computation of  $(\text{H.O.T.})_i^f(\mathbf{r}_{ij})$  in Eqs. (16) and (17), i.e.,

$$(\text{H.O.T.})_i^f(\mathbf{r}_{ij}) = (\text{H.O.T.})_i^{\bar{f}}(\mathbf{r}_{ij}) = f_{ij}^L - f_i - \bar{f}_i^1 \frac{\Delta x_{ij}}{h_i} - \bar{f}_i^2 \frac{\Delta y_{ij}}{h_i}, \quad (24)$$

Then Eqs. (16) and (17) can be rearranged into

$$\left( \frac{\partial f}{\partial x} \right)_i = \frac{1}{h_i} \sum_{j \in S_i} \alpha_{ij} (f_{ij} - f_{ij}^L) + \frac{\bar{f}_i^1}{h_i} \cdot \sum_{j \in S_i} \alpha_{ij} \frac{\Delta x_{ij}}{h_i} + \frac{\bar{f}_i^2}{h_i} \cdot \sum_{j \in S_i} \alpha_{ij} \frac{\Delta y_{ij}}{h_i}, \quad (25)$$

$$\left( \frac{\partial f}{\partial y} \right)_i = \frac{1}{h_i} \sum_{j \in S_i} \beta_{ij} (f_{ij} - f_{ij}^L) + \frac{\bar{f}_i^1}{h_i} \cdot \sum_{j \in S_i} \beta_{ij} \frac{\Delta x_{ij}}{h_i} + \frac{\bar{f}_i^2}{h_i} \cdot \sum_{j \in S_i} \beta_{ij} \frac{\Delta y_{ij}}{h_i}. \quad (26)$$

It can be proved with Eqs. (18) and (19) that there exist the following relations, i.e.,

$$\sum_{j \in S_i^k} \alpha_{ij} \frac{\Delta x_{ij}}{h_i} = 1, \quad \sum_{j \in S_i^k} \alpha_{ij} \frac{\Delta y_{ij}}{h_i} = 0, \quad \sum_{j \in S_i^k} \beta_{ij} \frac{\Delta x_{ij}}{h_i} = 0, \quad \sum_{j \in S_i^k} \beta_{ij} \frac{\Delta y_{ij}}{h_i} = 1. \quad (27)$$

By substituting the above relations into Eqs. (25) and (26), we can obtain

$$\left(\frac{\partial f}{\partial x}\right)_i = \overline{\left(\frac{\partial f}{\partial x}\right)}_i + \frac{1}{h_i} \sum_{j \in S_i} \alpha_{ij} (f_{ij} - f_{ij}^L), \quad (28)$$

$$\left(\frac{\partial f}{\partial y}\right)_i = \overline{\left(\frac{\partial f}{\partial y}\right)}_i + \frac{1}{h_i} \sum_{j \in S_i} \beta_{ij} (f_{ij} - f_{ij}^L). \quad (29)$$

Using Eqs. (28) and (29), the spatial derivatives in Eq. (1) can be expressed as

$$\left(\frac{\partial \mathbf{F}}{\partial x} + \frac{\partial \mathbf{G}}{\partial y}\right)_i = \overline{\left(\frac{\partial \mathbf{F}}{\partial x} + \frac{\partial \mathbf{G}}{\partial y}\right)}_i + \frac{1}{h_i} \sum_{j \in S_i} [\alpha_{ij} (\mathbf{F}_{ij} - \mathbf{F}_{ij}^L) + \beta_{ij} (\mathbf{G}_{ij} - \mathbf{G}_{ij}^L)]. \quad (30)$$

Equation (30) can be rearranged into

$$\left(\frac{\partial \mathbf{F}}{\partial x} + \frac{\partial \mathbf{G}}{\partial y}\right)_i = \overline{\left(\frac{\partial \mathbf{F}}{\partial x} + \frac{\partial \mathbf{G}}{\partial y}\right)}_i + \frac{1}{h_i} \sum_{j \in S_i} |\mathbf{S}_{ij}| (\mathbf{H}_{ij} - \mathbf{H}_{ij}^L) \cdot \mathbf{l}_{ij}, \quad (31)$$

where the inviscid flux terms are

$$\alpha_{ij} \mathbf{F}(\mathbf{U}_{ij}) + \beta_{ij} \mathbf{G}(\mathbf{U}_{ij}) = |\mathbf{S}_{ij}| \mathbf{H}_{ij} \cdot \mathbf{l}_{ij}, \quad \alpha_{ij} \mathbf{F}(\mathbf{U}_{ij}^L) + \beta_{ij} \mathbf{G}(\mathbf{U}_{ij}^L) = |\mathbf{S}_{ij}| \mathbf{H}_{ij}^L \cdot \mathbf{l}_{ij} \quad (32)$$

with

$$|\mathbf{S}_{ij}| = \sqrt{\alpha_{ij}^2 + \beta_{ij}^2}, \quad \mathbf{l}_{ij} = \frac{\alpha_{ij}}{\sqrt{\alpha_{ij}^2 + \beta_{ij}^2}} \mathbf{i} + \frac{\beta_{ij}}{\sqrt{\alpha_{ij}^2 + \beta_{ij}^2}} \mathbf{j}, \quad (33)$$

and

$$\mathbf{H} = \mathbf{F}(\mathbf{U})\mathbf{i} + \mathbf{G}(\mathbf{U})\mathbf{j}. \quad (34)$$

The numerical flux  $\mathbf{H}_{ij} \cdot \mathbf{l}_{ij}$  in Eq. (31) is then computed using a certain Riemann solver or flux-splitting technique associated with  $\mathbf{l}_{ij}$ , i.e.,

$$\mathbf{H}_{ij} \cdot \mathbf{l}_{ij} = \hat{\mathbf{H}}_{ij}(\mathbf{U}_{ij}^L, \mathbf{U}_{ij}^R, \mathbf{l}_{ij}). \quad (35)$$

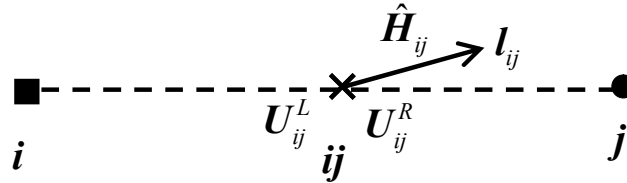


Fig. 3. Schematic of the upwind numerical flux.

In this paper, the numerical flux is approximated using the Roe approximate Riemann solver [30]. It is noted that this approach can result in the upwind fluxes which is suitable to deal with compressible flows. The related geometrical setup of the upwind numerical flux is shown in Fig. 3. If the numerical flux is evaluated using the flow variables as  $\mathbf{U}_{ij}^L = \mathbf{U}_i$  and  $\mathbf{U}_{ij}^R = \mathbf{U}_j$ , then the spatial accuracy is limited to the first order. In order to obtain the high order GFD scheme, the left and right states ( $\mathbf{U}_{ij}^L, \mathbf{U}_{ij}^R$ ) on both side of the mid-point  $ij$  are computed using the high order reconstruction polynomials of the flow variable, i.e.,

$$\mathbf{U}_{ij}^L = \mathbf{U}_i(\mathbf{r}_{ij}), \quad \mathbf{U}_{ij}^R = \mathbf{U}_j(\mathbf{r}_{ij}), \quad (36)$$

where  $\mathbf{U}_i(\mathbf{r}_{ij})$  and  $\mathbf{U}_j(\mathbf{r}_{ij})$  are deduced from the reconstruction step.

It is noted that the unit vector  $\mathbf{l}_{ij}$  that defined by the least-squares behaves similar to the outward surface normal in the finite volume method. Generally speaking, the unit vector  $\mathbf{l}_{ij}$  is not aligned the radial direction  $\mathbf{r}_{ij}$ . In practical simulations, this misalignment does not produce any difficulties according to our experiences. The possible reason is that GFD scheme of Eq. (31) does not explicitly

related to the radial direction  $r_{ij}$ , which is used solely to determine the mid-points where the fluxes are evaluated. The schematic of the unit vector  $l_{ij}$  in the local cloud of points is shown in Fig. 4. It can be seen that for the most support points, the corresponding unit vector  $l_{ij}$  is well aligned with the radial direction  $r_{ij}$ .

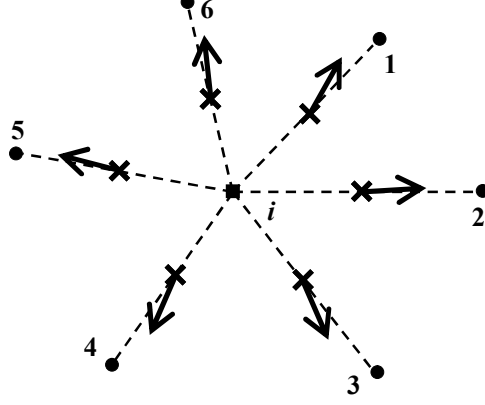


Fig. 4. Schematic of the unit vector  $l_{ij}$  in the local cloud of points.

### (3) Time integration step.

In the variational reconstruction procedure, the iterative solvers are used for solving the linear system to maintain the compactness of the solution procedure. If the linear system is required to reach convergence in every variational reconstruction step, the present high order GFD schemes are computationally expensive. To improve the computational efficiency, the reconstruction and implicit time integration coupled iterative technique proposed in [27] is used in the context of the present high order compact GFD schemes. The basic idea of the coupling iterative technique for steady-state and unsteady-state flows is briefly reviewed for completeness. For steady-state flow, as the convergence speed of the variational reconstruction is faster than that of the implicit time integration [27], the variational reconstruction can be iterated only once in each single time step and achieve convergence synchronously with implicit time integration. As the use of dual time stepping technique [31, 32] in the implicit time integration, the unsteady-state flow can be considered as a modified steady-state problem by advancing in pseudo time at each physical time step. The details of the coupling iterative procedure are described in the following.

By applying Eqs. (31)~(35) to Eq. (1), the semi-discretized high order GFD scheme for compressible Euler equations can be written as

$$\frac{\partial U_i}{\partial t} = - \left( \frac{\partial F}{\partial x} + \frac{\partial G}{\partial y} \right)_i - \frac{1}{h_i} \sum_{j \in S_i} |S_{ij}| \left[ \hat{H}_{ij}(U_{ij}^L, U_{ij}^R, l_{ij}) - H_{ij}^L \cdot l_{ij} \right] \equiv R(U_i). \quad (37)$$

**Table 1**

Coefficients of singly diagonally implicit, three-stage, 4th-order accurate Runge-Kutta method [33]. Parameter  $r = 1.06857902130163$ .

$r$	$r$		
$\frac{1}{2}$	$\frac{1}{2} - r$	$r$	
$1 - r$	$2r$	$1 - 4r$	$r$
	$\frac{1}{24 \left( \frac{1}{2} - r \right)^2}$	$1 - \frac{1}{12 \left( \frac{1}{2} - r \right)^2}$	$\frac{1}{24 \left( \frac{1}{2} - r \right)^2}$

The singly diagonally implicit, three-stage, 4th-order accurate Runge-Kutta (SDIRK) method [33] with dual time stepping LU-SGS [31, 32] is applied to achieve high order temporal accuracy. The semi-discretized scheme Eq. (37) can be integrated in time, i.e.,

$$\mathbf{U}_i^{n+1} = \mathbf{U}_i^n + \Delta t \sum_{k=1}^3 b_k \mathbf{R}(\mathbf{U}_{i,k}), \quad (38)$$

where each stage conservative variables  $\mathbf{U}_{i,k}$  is a function of a weighted sum of other intermediate residuals, i.e. ,

$$\mathbf{U}_{i,k} = \mathbf{U}_i^n + \Delta t \sum_{l=1}^k a_{kl} \mathbf{R}(\mathbf{U}_{i,l}). \quad (39)$$

The coefficients  $a_{kl}$  and  $b_k$  in Eqs. (39) and (38) are listed in **Table 1**. For each stage, Eq. (39) is implicit and nonlinear for the Euler equations. By introducing discretized pseudo time term into Eq. (39), we have

$$\frac{\mathbf{U}_{i,k}^{(m+1)} - \mathbf{U}_{i,k}^{(m)}}{\Delta \tau_i} + \frac{\mathbf{U}_{i,k}^{(m+1)} - \mathbf{U}_i^n}{\Delta t} = \sum_{l=1}^{k-1} a_{kl} \mathbf{R}(\mathbf{U}_{i,l}) + a_{kk} \mathbf{R}(\mathbf{U}_{i,k}^{(m+1)}), \quad (40)$$

where the pseudo time step  $\Delta \tau_i$  can be computed according to the local time step. The  $k$ -stage conservative variables  $\mathbf{U}_{i,k}$  can be solved using dual time stepping LU-SGS. In solving the Eq. (40), the iterative solver in Eq. (11) is solved only once in a pseudo-time step. The variational reconstruction and the implicit dual time stepping technique coupled solution procedure is summarized in **Algorithm 1** for the advancement in one physical time step.

---

**Algorithm 1** Unsteady flow solver using coupled iteration method in one physical time step.

---

Initialize  $\mathbf{U}_{i,1}^{(0)}$  with  $\mathbf{U}_i^n$  for each inner point  $i$

Do  $k = 1, 3$

    Initialize  $\mathbf{U}_{i,k}^{(0)}$  with  $\mathbf{U}_{i,k-1}$  for each inner point  $i$

    Do  $m = 1, \text{inner\_iter\_step\_max}$

1. Reconstruction for each inner point  $i$  as well as the boundary points
2. Correct the boundary points' value with boundary conditions
3. Compute  $\mathbf{R}(\mathbf{U}_{i,k}^{(m)})$  for each inner point  $i$
4. Compute  $\mathbf{U}_{i,k}^{(m+1)}$  for each inner point  $i$  with Eq. (40)
5. Compute the density residual( $m$ )
6. If residual( $m$ )/residual(1) <  $\mathcal{E}$  Exit

    End Do

End Do

7. Compute  $\mathbf{U}_i^{n+1}$  with Eq. (38) for each inner point  $i$  as well as the boundary points

---

It can be seen from **Algorithm 1** that the variational reconstruction is carried only once in a point by point manner in each pseudo time step. The coupling of the variational reconstruction with the dual time stepping diagonally implicit Runge–Kutta method is in fact very close to performing the reconstruction in [24] in a dual time stepping implicit scheme. Therefore, by using the coupled iteration method, the implicit property of the variational reconstruction does not lead to any extra computational cost. Furthermore, the boundary treatment has been added into **Algorithm 1** for the sake of completeness. It should be noted that both the flow variables of the inner points are updated with the diagonally implicit Runge–Kutta method. For the boundary points, the conservative variables  $\mathbf{U}_{i,k}$  in each stage are computed using the boundary points' variation reconstruction, which will be given in the next section. If  $\mathbf{U}_{i,k}$  are obtained, the corresponding right hand term  $\mathbf{R}(\mathbf{U}_{i,k})$  can be

computed with Eq. (39). Then the conservative variables  $U_i^{n+1}$  at boundary points can be expressed as

$$U_i^{n+1} = U_i^n + \sum_{k=1}^3 b_k M^{-1} \Delta U_{i,k}, \quad (41)$$

where  $M^{-1}$  is the inverse of the matrix  $M$  that is formed with coefficients  $a_{kl}$  in Butcher table (see Table 1).

### 2.3 Boundary treatment with variational reconstruction

The flow variables of the inner points in each stage of the diagonally implicit Runge–Kutta method are updated through the time integration. This is not the case for the flow variables at the boundary nodal points. The updating of the flow variables at these points needs not only to utilize the information of the inner points nearby but also to satisfy the corresponding boundary conditions. The implementation of boundary conditions is of critical importance to maintain the overall accuracy of the numerical schemes.

In our previous work [24], the high order boundary treatment consists of two steps, i.e., the extrapolation-correction step and the gradient reconstruction step. Firstly, the values of the boundary points are obtained from the interior points with high order extrapolation and then corrected to enforce corresponding boundary conditions. Secondly, the distributions of the flow variables at these boundary points are obtained in terms of the corrected values at the boundary points as well as the values of the interior points. The stencils corresponding to these two steps are different and both could be very large, as shown in Fig. 5. To circumvent the large stencil problem, a new high order boundary treatment technique is proposed and the details are given in the following.

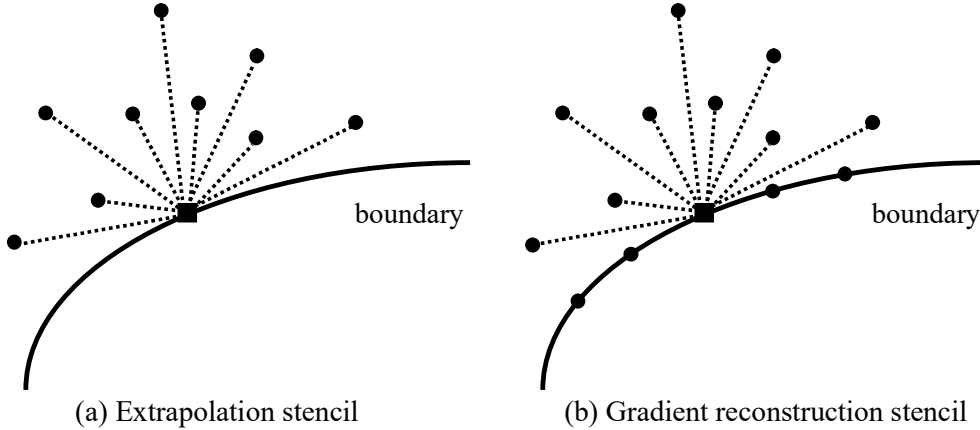


Fig. 5. Schematic of the boundary stencil points in our previous work [24].

If the values of the inner points have been updated through the time integration, the flow variables at the boundary points can be extrapolated from the inner points. Specifically, let  $u_{i_b}$  stand for the flow variable at the boundary point  $i_b$ , the flow variable distribution  $u_{i_b}(\mathbf{r})$  around the boundary point  $i_b$  can be approximated by a degree  $k$  polynomial defined by

$$u_{i_b}(\mathbf{r}) = u_{i_b}^0 + \sum_{l=1}^K u_{i_b}^l \phi_l^l(\mathbf{r}), \quad (42)$$

where  $u_{i_b}^l$  ( $l = 0, 1, 2, \dots, K$ ) denotes the unknown coefficients of the polynomial. Unlike the reconstruction in the inner points, here  $u_{i_b}^0$  is the unknown boundary extrapolation value.

As the variational reconstruction method always provides enough information, the boundary treatment can also be implemented on compact support points. The cost function of the boundary node is defined as

$$\begin{aligned}
J_{i_b} = \sum_{j \in S_{i_b}} w_{i_b j} & \left\{ \left( u_{i_b}(\mathbf{r}_{i_b j}) - u_j(\mathbf{r}_{i_b j}) \right)^2 + \Delta r_{i_b j}^2 \left[ \left( u_{i_b, x}(\mathbf{r}_{i_b j}) - u_{j, x}(\mathbf{r}_{i_b j}) \right)^2 \right. \right. \\
& \left. \left. + \left( u_{i_b, y}(\mathbf{r}_{i_b j}) - u_{j, y}(\mathbf{r}_{i_b j}) \right)^2 \right] + \Delta r_{i_b j}^4 \left[ \left( u_{i_b, xx}(\mathbf{r}_{i_b j}) - u_{j, xx}(\mathbf{r}_{i_b j}) \right)^2 \right. \right. \\
& \left. \left. + \left( u_{i_b, xy}(\mathbf{r}_{i_b j}) - u_{j, xy}(\mathbf{r}_{i_b j}) \right)^2 + \left( u_{i_b, yy}(\mathbf{r}_{i_b j}) - u_{j, yy}(\mathbf{r}_{i_b j}) \right)^2 \right] + \dots \right\}.
\end{aligned} \tag{43}$$

where the weights  $w_{i_b j}$  are the same as those defined in Eq. (5). The unknown coefficients  $u_{i_b}^l$  ( $l = 0, 1, 2, \dots, K$ ) can be determined by the minimizing the cost function, i.e.,

$$\frac{\partial J_{i_b}}{\partial u_{i_b}^q} = 0, \quad q = 0, 1, 2, \dots, K. \tag{44}$$

The solution procedure is similar to that used in the reconstruction step for the inner points and thus is omitted here. As the boundary extrapolation value  $u_{i_b}^0$  has been obtained, it needs to be corrected to enforce the corresponding boundary conditions. In this paper, the boundary conditions based on extrapolation of the characteristic variables (BCECV) [34] is used. For the inviscid solid wall, the primitive variables  $(\rho, u, v, p)_{i_b}$  are corrected by

$$\begin{cases} \rho_{i_b} = \rho_{i_b}^0 - \tilde{\rho}_{i_b} (n_x u_{i_b}^0 + n_y v_{i_b}^0) / \tilde{a}_{i_b} \\ u_{i_b} = u_{i_b}^0 - n_x (n_x u_{i_b}^0 + n_y v_{i_b}^0) \\ v_{i_b} = v_{i_b}^0 - n_y (n_x u_{i_b}^0 + n_y v_{i_b}^0) \\ p_{i_b} = p_{i_b}^0 - \tilde{\rho}_{i_b} \tilde{a}_{i_b} (n_x u_{i_b}^0 + n_y v_{i_b}^0) \end{cases}, \tag{45}$$

where  $\tilde{\rho}_{i_b}$  is the reference density,  $\tilde{a}_{i_b}$  is the reference speed of sound,  $(n_x, n_y)$  is the unit normal vector pointing out of the computational domain. The reference state is set to be equal to the boundary extrapolated value.

It is noted that the boundary treatment with variational reconstruction can use more information than our previous work [24]. By the introduction of the boundary cost function, the extrapolation can be solved seamlessly together with the reconstruction of the non-boundary points. Furthermore, this extrapolation technique makes both the value of the extrapolated variable and its derivatives combined into one single step. Therefore, the new boundary treatment is more flexible.

## 2.4 WBAP limiter

The WBAP limiter [24, 35, and 36] is used to suppress non-physical numerical oscillations near discontinuities. Similar to the limiting procedure of the WENO schemes [37-38], several candidate reconstruction polynomials need to be provided on the reference point. Candidate polynomials for the WBAP limiter are obtained with the so-called secondary reconstruction (SR) technique. The SR uses the continuations of the reconstruction polynomials on neighboring support points of the current reference point as the additional candidate polynomials. The resulting candidate polynomials with SR can be expressed as

$$u_{j \rightarrow i}(\mathbf{r}) = u_i + \sum_{l=1}^K u_{j \rightarrow i}^l \phi_i^l(\mathbf{r}), \quad j \in S_i, \tag{46}$$

where  $u_{j \rightarrow i}^l$  is the coefficient of SR. In the WBAP limiter, the limited reconstruction polynomial  $\tilde{u}_i(\mathbf{r})$  is computed by a non-linear average of  $u_i(\mathbf{r})$  and  $u_{j \rightarrow i}(\mathbf{r})$  in the form

$$\tilde{u}_i(\mathbf{r}) = u_i + \sum_{l=1}^K \tilde{u}_i^l \phi_i^l(\mathbf{r}), \quad \tilde{u}_i^l = L(u_i^l, u_{j \rightarrow i}^l), \quad j \in S_i, \tag{47}$$

where  $\tilde{u}_i^l$  is the coefficients after limited, and the limiting function is given by

$$L(a_0, a_1, \dots, a_J) = a_0 \cdot \tilde{L}(1, \frac{a_1}{a_0}, \dots, \frac{a_J}{a_0}) = a_0 \cdot \tilde{L}(1, \theta_1, \dots, \theta_J). \quad (48)$$

with

$$\tilde{L}(1, \theta_1, \dots, \theta_J) = \frac{n_p + \sum_{m=1}^J \theta_j^{1-p}}{n_p + \sum_{m=1}^J \theta_j^{-p}}, \quad p = 4, \quad n_p = 10. \quad (49)$$

The WBAP limiter is applied in a successive manner in terms of the characteristic variables. The key ingredient of the successive limiting procedure is to apply the limiter to high order derivatives first over the entire domain and the lower order derivatives of the SRs are evaluated in terms of the already limited high order derivatives. This approach yields a very robust limiting procedure. Further details of the property and implementation of the WBAP limiter can be found in [24, 35, and 36]. Furthermore, it should be noted that the limiting procedure is applied after obtaining the distribution of the flow variables. The flux evaluation is also affected by the limiter since the left/right states of the Riemann problems are computed using the limited reconstruction polynomials.

### 3 Numerical examples

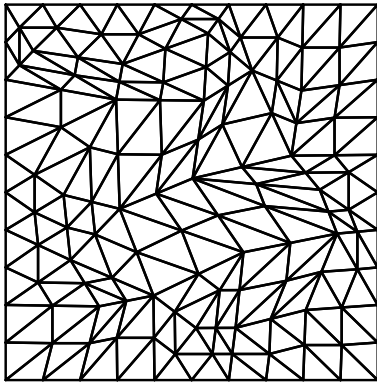
Several numerical test cases are computed to demonstrate the performance of the proposed high order GFD schemes. The primitive variables  $(\rho, u, v, p)$  are used in the reconstruction step as well as the boundary treatment. In simulations of all the test cases, the parameter  $Z$  defined in the weighted function (see Eqs. (5), (15) and (43)) is set to 2, and the boundary points' weight  $\hat{\omega}_b$  is set to 1.

#### 3.1 Isentropic vortex problem

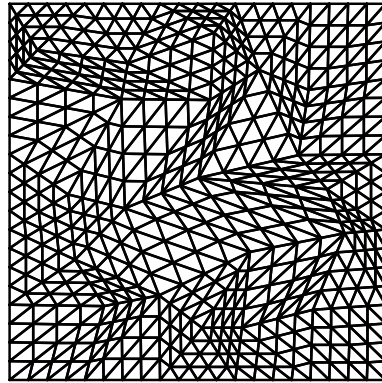
This test case [38] is selected to verify the accuracy and efficiency of the proposed high order GFD schemes in computing two-dimensional flows without shock waves. The mean flow is  $\rho_\infty = 1$ ,  $p_\infty = 1$ , and  $(u_\infty, v_\infty) = (1, 1)$ . An isentropic vortex is added to the mean flow with the perturbations,

$$(\delta u, \delta v) = \frac{\chi}{2\pi} e^{\frac{1-r^2}{2}(-\bar{y}, \bar{x})}, \quad \delta T = -\frac{(\gamma-1)\chi^2}{8\gamma\pi^2} e^{1-r^2}, \quad \delta S = 0. \quad (50)$$

where  $(\bar{x}, \bar{y}) = (x-5, y-5)$ ,  $r^2 = \bar{x}^2 + \bar{y}^2$ , and the vortex strength  $\chi = 5$ . If the computational domain is infinite large, the exact solution is just the convection of the initial condition as the speed of the mean flow velocity.



(a) Mesh 1 ( $N_e=232$ )



(b) Mesh 2 ( $N_e=928$ )

Fig. 6. Meshes used for the isentropic vortex problem (Mesh 1 and Mesh 2).

The computational domain is taken as  $[0, 10] \times [0, 10]$  with the periodic boundaries and divided into irregular triangular elements, as shown in Fig. 6. The computation is carried out until  $t=2.0$  using the 2nd and 3rd order GFD schemes with variation reconstruction (V-GFD). The meshes are the same as those used in **Section 3.1** suitably scaled for the new spatial domain. The CFL number for the local pseudo time step is set to 40, and the convergence criterion for the inner iteration is  $\varepsilon = 10^{-5}$ . The physical time step  $\Delta t$  is set to 0.40, 0.20, 0.10, 0.05, and 0.025 on Mesh 1 to Mesh 5, respectively. The  $L_1$  and  $L_\infty$  norms of the errors in density as well as the CPU time for the isentropic vortex problem are listed in **Table 2**. The accuracy results using the 2nd and 3rd order GFD schemes with least-squares' reconstruction (LS-GFD) in our previous work [24] using SDIRK+LU-SGS are also listed for comparison. The error norms versus the length scale are shown in Fig. 7. The length scale  $h$  in **Table 2** is define as

$$h \sim \frac{1}{\sqrt{N_e}}, \quad (51)$$

where  $N_e$  is the number of mesh elements.

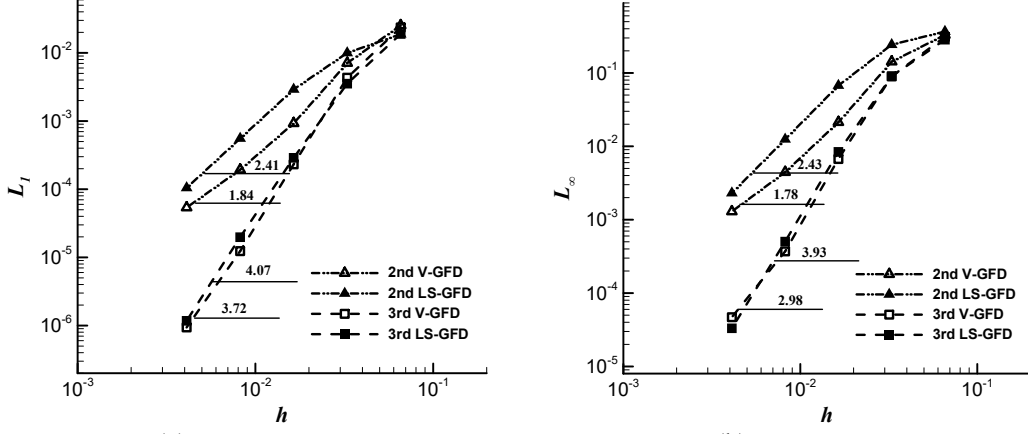
**Table 2**  
Accuracy test for the isentropic vortex problem at  $t=2.0$ .

Schemes	$h$	$L_1$ norm	Order	$L_\infty$ norm	Order	CPU time (s)
2nd V-GFD	6.57E-02	2.53E-02	-	3.30E-01	-	7.8E-02
	3.28E-02	7.10E-03	1.83	1.43E-01	1.21	0.55
	1.64E-02	9.28E-04	2.93	2.13E-02	2.74	4.62
	8.21E-03	1.93E-04	2.26	4.45E-03	2.26	55.19
	4.10E-03	5.38E-05	1.84	1.29E-03	1.78	548.69
3rd V-GFD	6.57E-02	2.36E-02	-	3.10E-01	-	1.1E-01
	3.28E-02	4.32E-03	2.45	8.97E-02	1.79	0.92
	1.64E-02	2.32E-04	4.22	6.71E-03	3.74	7.69
	8.21E-03	1.24E-05	4.23	3.70E-04	4.18	85.33
	4.10E-03	9.39E-07	3.72	4.69E-05	2.98	693.83
2nd LS-GFD	6.57E-02	1.88E-02	-	3.67E-01	-	7.8E-02
	3.28E-02	9.99E-03	0.91	2.43E-01	0.59	0.64
	1.64E-02	2.92E-03	1.78	6.74E-02	1.85	5.69
	8.21E-03	5.56E-04	2.39	1.25E-02	2.43	63.59
	4.10E-03	1.05E-04	2.41	2.31E-03	2.43	631.27
3rd LS-GFD	6.57E-02	1.89E-02	-	2.84E-01	-	0.13
	3.28E-02	3.54E-03	2.42	9.01E-02	1.66	0.95
	1.64E-02	2.89E-04	3.62	8.41E-03	3.42	8.85
	8.21E-03	1.98E-05	3.87	5.04E-04	4.06	92.37
	4.10E-03	1.17E-06	4.07	3.31E-05	3.93	760.27

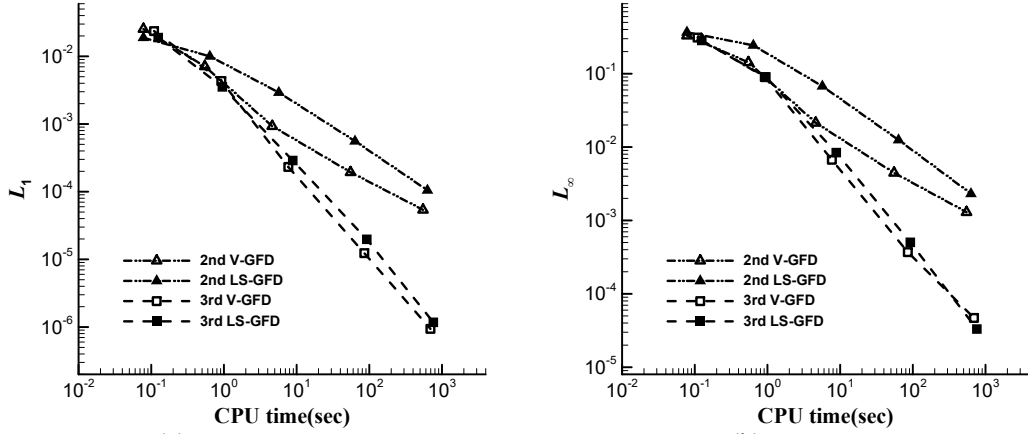
The results in **Table 2** and Fig. 7 show that the  $L_1$  and  $L_\infty$  error norms in both V-GFD and LS-GFD schemes can reach the nominal order of accuracy. The solutions computed by 2nd V-GFD scheme are much more accurate than those computed by 2nd LS-GFD scheme. Furthermore, it should be noted that both 3rd order V-GFD and LS-GFD schemes can achieve nearly one order higher than their nominal order of accuracy in terms of the  $L_1$  error norm.

The efficiency comparison can be deduced from **Table 2**. The solution CPU time versus the  $L_1$  and  $L_\infty$  error norms are plotted in Fig. 8. It can be seen that the V-GFD schemes (especially the 2nd V-

GFD scheme) can achieve the same accuracy using less CPU time, which means that the V-GFD schemes are more efficient than the LS-GFD schemes of the same level of accuracy. Furthermore, the 3rd order V-GFD scheme is more efficient than the 2nd order V-GFD scheme at the high accuracy level on sufficiently fine meshes. For example, the third order V-GFD scheme on Mesh 4 is more than one order of magnitude in accuracy and more efficient compared with the 2nd order V-GFD scheme.



(a)  $L_1$  error norm (b)  $L_\infty$  error norm  
Fig. 7. Error norms versus the length scale for the isentropic vortex problem.



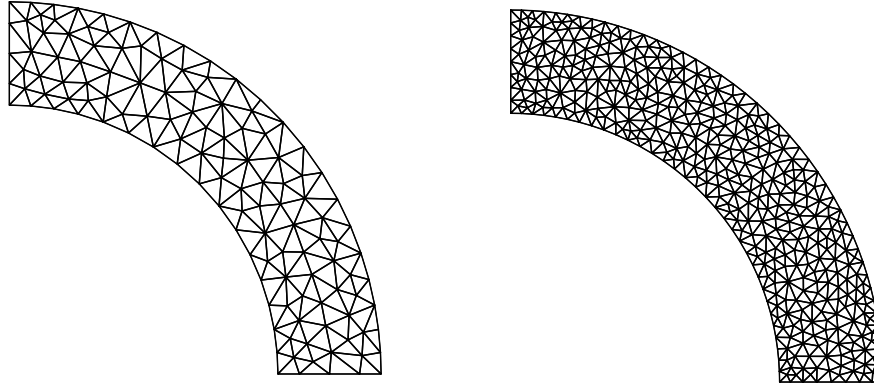
(a)  $L_1$  error norm (b)  $L_\infty$  error norm  
Fig. 8. Error norms versus CPU time for the isentropic vortex problem.

### 3.2 Supersonic vortex flow problem

This test case [39-40] is considered to verify the accuracy of the proposed high order V-GFD schemes in solving problems with physical boundaries and the results are compared with those computed by high order LS-GFD schemes. We consider an isentropic supersonic vortex flow between two concentric circular arcs of radii  $r_i = 1$  and  $r_o = 1.384$  in the first quadrant, whose exact solution is given in non-dimensional form by

$$\rho = \rho_i \left[ 1 + \frac{\gamma-1}{2} M_i^2 \left( 1 - \frac{r_i^2}{r^2} \right) \right]^{\frac{1}{\gamma-1}}, \quad U = \frac{c_i M_i}{r}, \quad u = \frac{yU}{r}, \quad v = -\frac{xU}{r}, \quad p = \frac{\rho^\gamma}{r}. \quad (52)$$

At the inner boundary, the Mach number  $M_i$  is set to 2.25, the density  $\rho_i$  is set to 1.0, and the sound speed at the inner boundary  $c_i$  can be computed as 1.0.



(a) Mesh 1 ( $N_e=205$ ) (b) Mesh 2 ( $N_e=772$ )  
 Fig. 9. Meshes used for the supersonic vortex problem (Mesh 1 and Mesh 2).

**Table 3**

Accuracy test for the supersonic vortex problem.

Schemes	$h$	$L_1$ norm	Order	$L_2$ norm	Order
2nd V-GFD	6.98E-02	3.52E-03	-	4.55E-03	-
	3.77E-02	6.78E-04	2.67	1.00E-03	2.46
	1.85E-02	9.45E-05	2.76	1.37E-04	2.78
	9.20E-03	1.87E-05	2.33	2.55E-05	2.41
3rd V-GFD	6.98E-02	2.80E-03	-	4.76E-03	-
	3.77E-02	1.04E-04	5.36	1.34E-04	5.80
	1.85E-02	8.54E-06	3.49	1.18E-05	3.40
	9.20E-03	5.02E-07	4.07	8.44E-07	3.79
2nd LS-GFD	6.98E-02	6.08E-03	-	9.08E-03	-
	3.77E-02	1.80E-03	1.97	2.76E-03	1.93
	1.85E-02	2.44E-04	2.80	4.18E-04	2.64
	9.20E-03	2.88E-05	3.06	5.77E-05	2.84
3rd LS-GFD	6.98E-02	4.77E-03	-	7.60E-03	-
	3.77E-02	3.34E-04	4.32	5.61E-04	4.23
	1.85E-02	2.39E-05	3.69	3.41E-05	3.92
	9.20E-03	1.07E-06	4.46	1.61E-06	4.39

Four different unstructured meshes (from Mesh 1 to Mesh 4) containing 205, 772, 2930, and 11808 mesh elements are employed (see Fig. 9). Each mesh has almost four times more mesh elements than the immediate coarser level and uniform refinement has been applied in the mesh generation. The computation is carried out using the 2nd and 3rd order V-GFD and LS-GFD schemes. All computations are performed until the solution reaches the residual being less than  $10^{-12}$ . The  $L_1$  and  $L_2$  error norms in density for the supersonic vortex flow problem are listed in **Table 3**. The  $L_1$  and  $L_2$  error norms versus the length scale are shown in Fig. 10. The results in **Table 3** and Fig. 10 show all the schemes can reach the nominal order of accuracy and the solutions computed by V-GFD schemes are much more accurate than those computed by LS-GFD schemes. Furthermore, it should be noted that both 3rd order V-GFD and LS-GFD schemes can achieve nearly one order higher than their nominal order of accuracy.

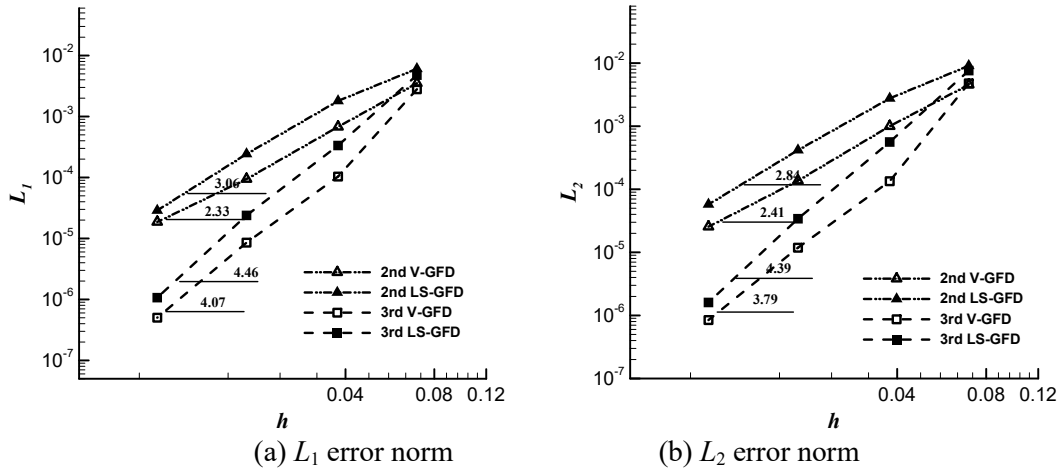


Fig. 10. Error norms versus the length scale for the supersonic vortex problem.

### 3.3 Subsonic flow around around the NACA0012 airfoil

An inviscid subsonic flow around the NACA0012 airfoil is considered to investigate the convergence performance of the proposed high order V-GFD schemes for steady flow simulation and the results are compared with those computed by high order LS-GFD schemes. The free stream Mach number is  $M = 0.63$  and the angle of attack  $\alpha = 2.0^\circ$ . The far-field is located at 30 chords length. The unstructured mesh used in this test case is shown in Fig. 11, which consists of 30 096 mesh elements, and 226 wall boundary points.

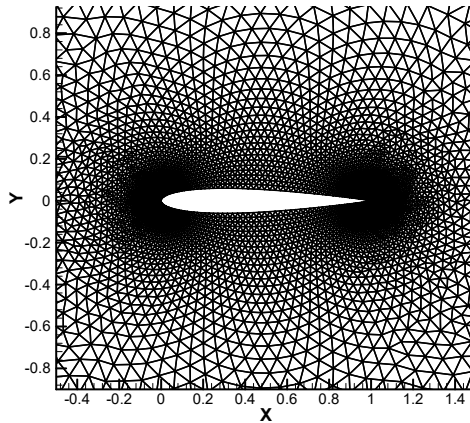


Fig. 11. Unstructured mesh used for subsonic flows around the NACA0012 airfoil.

The computation is carried out using 2nd and 3rd V-GFD and LS-GFD schemes. All computations are started with uniform flow. The CFL number for the local pseudo time step is set to 40. The comparison of convergence histories is shown in Fig. 12. The results in Fig. 12 show that the residuals of all the schemes can drop to  $10^{-12}$ , which demonstrates the superior convergence property of these schemes. Compared with LS-GFD schemes of the same order of accuracy, V-GFD schemes require less iterations and CPU time to reach steady-state solution.

The convergence histories in terms of the  $L_1$  entropy error norm is shown in Fig. 13 to compare the computational efficiency. It can be seen that the 2nd V-GFD scheme can obtain much more accurate solutions than that of the 2nd LS-GFD scheme using nearly the same CPU time, which indicates that the 2nd V-GFD scheme is more efficient than the 2nd LS-GFD scheme. The 3rd V-GFD and LS-GFD schemes obtain nearly the same accurate solutions and more accurate than that of the 2nd schemes.

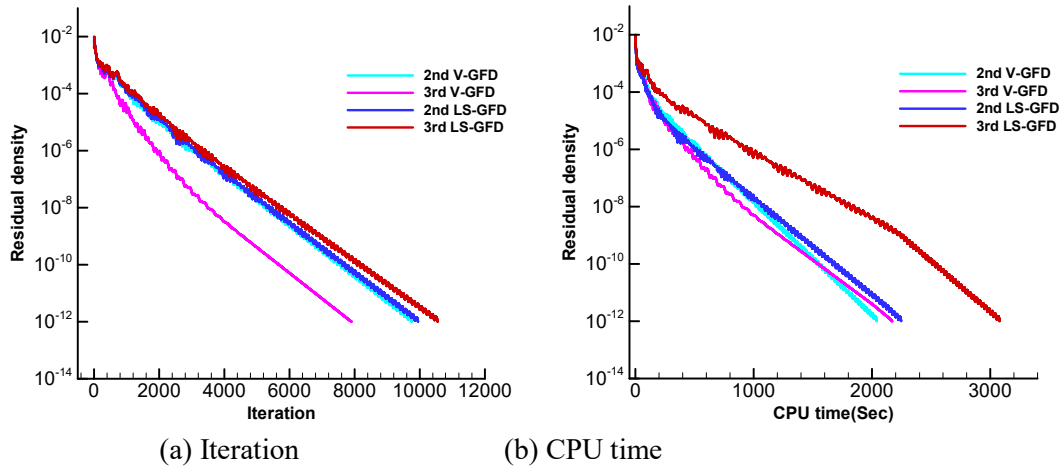


Fig. 12. Comparison of the convergence history for subsonic flows around the NACA0012 airfoil.

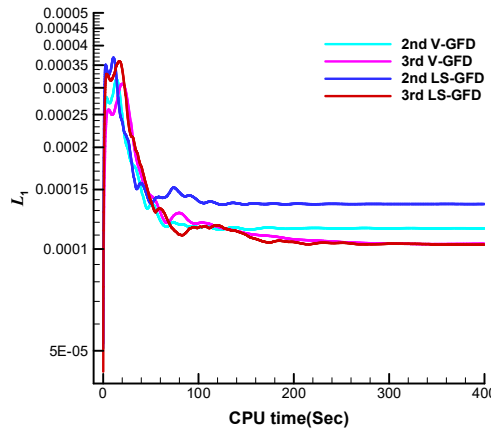
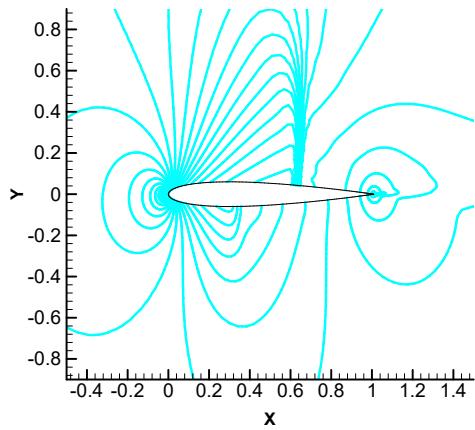


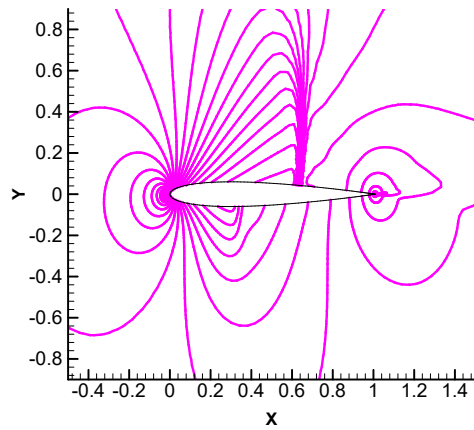
Fig. 13. Entropy error comparison for subsonic flows around the NACA0012 airfoil.

### 3.4 Transonic flow around around NACA0012 airfoil

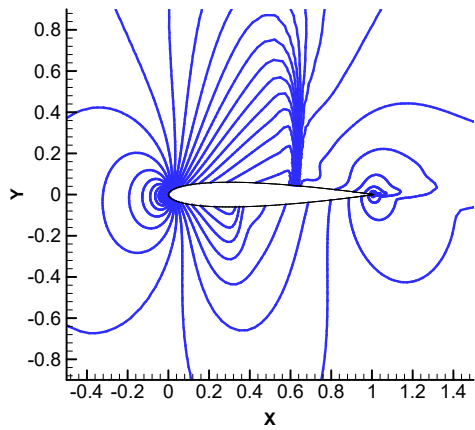
This test case is chosen to demonstrate the ability of the proposed high order V-GFD schemes in simulation of transonic flows around the NACA0012 airfoil with strong and weak shock waves and the results are compared with those computed by high order LS-GFD schemes. The free stream Mach number is  $M = 0.8$  and the angle of attack  $\alpha = 1.25^\circ$ . The comparisons of the pressure and Mach counters are shown in Figs. 14 and 15. The comparison of the surface pressure coefficients is shown in Fig. 16. It can be seen that the solutions using V-GFD schemes capture sharper shock waves and more accurate position of the waves compared with LS-GFD schemes of the same order of accuracy. No-oscillatory solutions are found in the V-GFD schemes, and there exists slight oscillatory in the 3rd LS-GFD scheme.



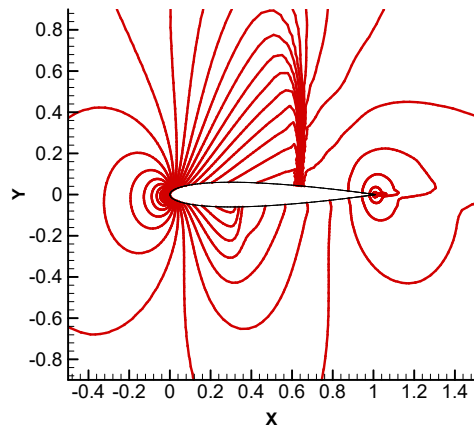
(a) 2nd V-GFD



(b) 3rd V-GFD

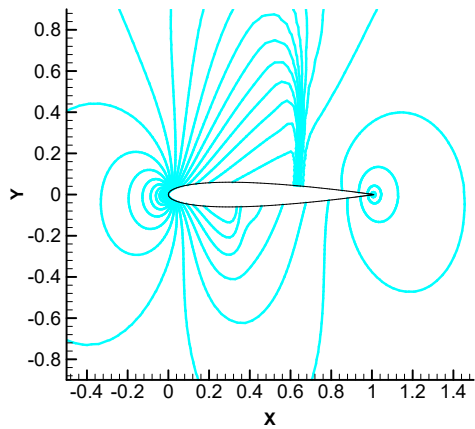


(c) 2nd LS-GFD

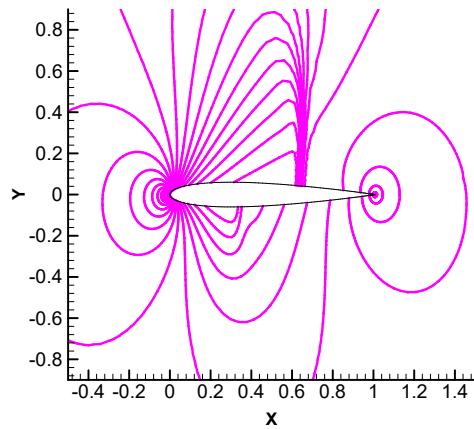


(d) 3rd LS-GFD

Fig. 14. Comparison of the Mach counters for transonic flows around the NACA0012 airfoil.



(a) 2nd V-GFD



(b) 3rd V-GFD

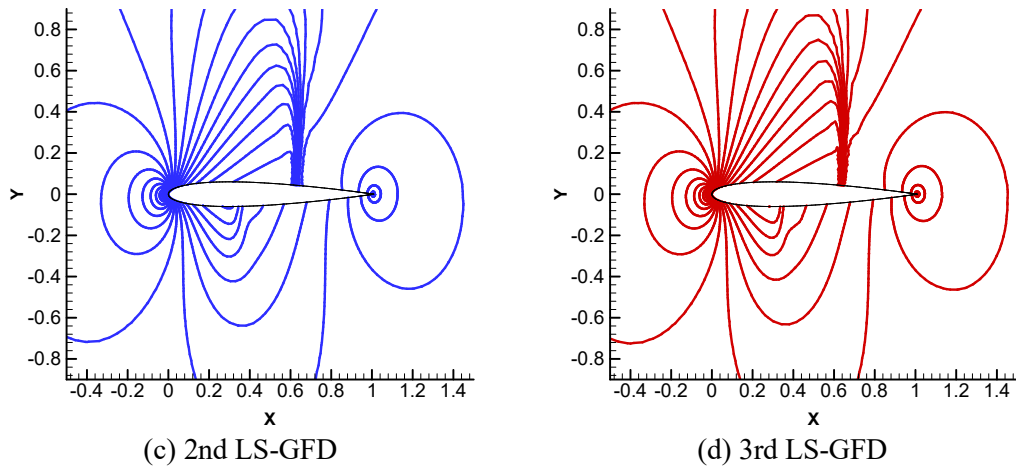


Fig. 15. Comparison of the pressure counters for transonic flows around the NACA0012 airfoil.

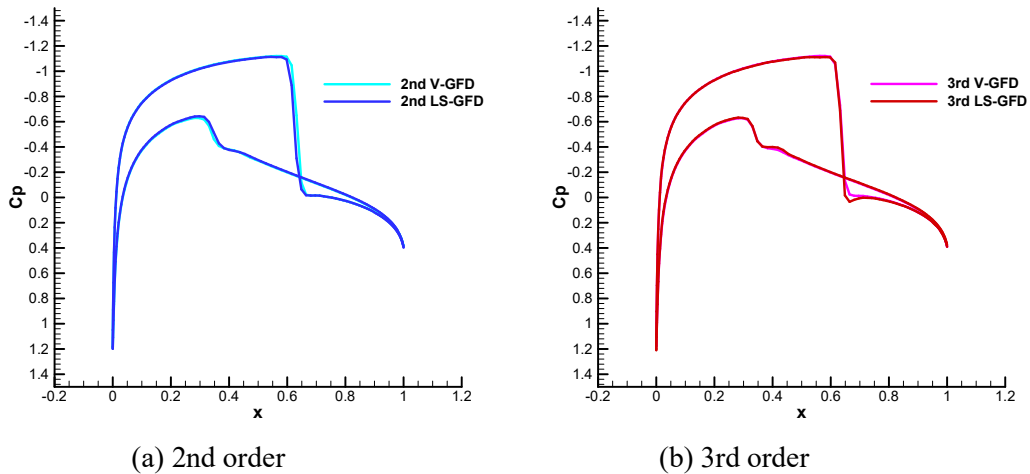


Fig. 16. Comparison of the surface pressure coefficients for transonic flows around the NACA0012 airfoil.

## 4 Conclusions

This paper proposes a general framework for constructing the high order compact GFD method. The variational method is used in both the reconstruction and a hybrid approach is used for the flux evaluation procedures in terms of up to 3rd order polynomials to achieve high order accuracy on a compact stencil. The WBAP limiter based on the secondary reconstruction which was originally designed for the high order finite volume methods on unstructured grids is successfully extended to the high order compact GFD method. A new flexible high order boundary treatment with the variational method is proposed to implement the boundary conditions in high order of accuracy. The numerical results demonstrate the high order accuracy, high resolution, and shock capturing capability of the proposed high order compact GFD schemes.

## References

- [1] Batina J.T., A gridless Euler/Navier-Stokes solution algorithm for complex-aircraft applications,

- AIAA Paper 1993; 93-0333.
- [2] Katz A, Jamenson A. A comparison of various meshless schemes within a unified algorithm. AIAA Paper 2009; 2009-596.
- [3] Katz A, Jameson A. Meshless scheme based on alignment constraints. AIAA Journal 2010; 2501-2511.
- [4] Hashemi Y, Jahangirian A. Implicit fully mesh-less method for compressible viscous flow calculations. J Comput Appl Math 2011; 235: 4687-4700.
- [5] Su XR, Yamamoto S, Nakahashi K. Analysis of a meshless solver for high Reynolds number flow. J Comput Phys 2013; 72: 505-527.
- [6] Sundar DS, Yeo KS. A high order meshless method with compact support. J Comput Phys 2014; 272: 70-87.
- [7] Ding H, Shu C, Yeo KS. Development of least-square-based two-dimensional finite-difference schemes and their application to simulate natural convection in a cavity. Comput Fluids 2004; 33: 137-154.
- [8] Tota PV, Wang ZJ. Meshfree Euler solver using local radial basis functions for inviscid compressible flows. AIAA Paper 2007; 2007-4581.
- [9] Jaisankar S, Shivashankar K, Raghurama Rao SV. A grid-free central scheme for inviscid compressible flows. AIAA Paper 2007; 2007-3946.
- [10] Anandhanarayanan K, Krishnamurthy R, Debasis Chakraborty. Development and validation of a grid-free viscous solver. AIAA Journal 2016; 3310-3313.
- [11] Liu JL, Su SJ. A potentially gridless solution method for the compressible Euler/Navier-Stokes equation. AIAA Paper 1996; 96-0526.
- [12] Kirshman DJ, Liu F. Gridless boundary condition treatment for a non-body-conforming mesh. AIAA Paper 2002; 2002-3285.
- [13] Koh EPC, Tsai HM. Euler solution using cartesian grid with a gridless least-squares boundary treatment. AIAA Journal 2005; 246-255.
- [14] Luo H, and Baum JD, Löhner R. A Hybrid Building-Block and Gridless Method for Compressible Flows. AIAA Paper 2006; 2006-3710.
- [15] Ma ZH, Chen HQ, Zhou CH. A study of point moving adaptivity in gridless method. Comput. Methods Appl. Mech. Engrg. 2008; 197: 1926–1937.
- [16] Sridar D, Balakrishnan N. An upwind finite difference scheme for meshless solvers. J Comput Phys 2003; 189: 1-29.
- [17] Munikrishna N, Balakrishnan N. Turbulent flow computations on a hybrid Cartesian point distribution using meshless solver LSF-DU. Computers & Fluids 2011; 40(1): 118–138.
- [18] Oñate E, Idelsohn S, Zienkiewicz OC. A stabilized finite point method for analysis of fluid mechanics problems. Comput. Methods Appl. Mech. Engrg. 1996; 139: 315-346.
- [19] Löhner R, Sacco C, Oñate E and Idelsohn S. A finite point method for compressible flow. Int J Numer Meth Eng 2002; 53: 1765-1779.
- [20] Ortega E, Oñate E, Idelsohn S. A finite point method for adaptive three-dimensional compressible flow calculations. Int. J. Numer. Meth. Fluids 2009; 60:937–971.
- [21] Ortega E, Oñate E, Idelsohn S, Flores F. Application of the finite point method to high-Reynolds number compressible flow problems. Int. J. Numer. Meth. Fluids 2014; 74:732–748.
- [22] Chung KC. A generalized finite-difference method for heat transfer problems of irregular geometries. Numerical Heat Transfer 1981, 4: 345-357.
- [23] Shu C, Ding H, Chen HQ, Wang TG. An upwind local RBF-DQ method for simulation of inviscid compressible flows. Comput. Methods Appl. Mech. Engrg. 2005; 194: 2001–2017.
- [24] Li XL, Ren YX, Li W. Construction of the high order accurate generalized finite difference schemes for inviscid compressible flows. Commun Comput Phys (accepted).
- [25] R. Abgrall, A. Larat, M. Ricchiuto, Construction of very high order residual distribution schemes for steady inviscid flow problems on hybrid unstructured meshes, J. Comput. Phys. 230(11) (2011) 4103–4136.
- [26] L. Zhang, W. Liu, L. He, X. Deng, H. Zhang, A class of hybrid DG/FV methods for conservation laws I: basic formulation and one-dimensional systems, J. Comput. Phys. 231(4) (2012) 1081–1103.
- [27] Q. Wang, Y.X. Ren, W. Li, Compact high order finite volume method on unstructured grids II:

- extension to two-dimensional Euler equations, *J. Comput. Phys.* 314 (2016) 883–908.
- [28] Q. Wang, Y.X. Ren, W. Li, Compact high order finite volume method on unstructured grids III: variational reconstruction, *J. Comput. Phys.* 337 (2017) 1–26.
- [29] E.F. Toro, V.A. Titarev, Derivative Riemann solvers for systems of conservation laws and ADER methods, *J. Comput. Phys.* 212 (2006) 150–165.
- [30] Roe P. Approximate Riemann solvers, parameter vectors, and difference schemes. *J Comput Phys* 1981; 43(2): 357-372.
- [31] A. Arnone, M.S. Liou, L.A. Povinelli, Integration of Navier–Stokes equations using dual time stepping and a multigrid method, *AIAA J.* 33(6) (1995) 985–990.
- [32] L.P. Zhang, Z.J. Wang, A block LU-SGS implicit dual time-stepping algorithm for hybrid dynamic meshes, *Comput. Fluids* 33(7) (2004) 891–916.
- [33] L. Ferracina, M.N. Spijker, Strong stability of singly-diagonally-implicit Runge–Kutta methods, *Appl. Numer. Math.* 58(11) (2008) 1675–1686.
- [34] Sun Z.S., Ren Y.X., Zha B., et al. High order boundary conditions for high order finite difference schemes on curvilinear coordinates solving compressible flows. *J Sci Comput* 2015; 65: 790-820.
- [35] Li W, Ren YX, Guo D, Hong Luo. The multi-dimensional limiters for solving hyperbolic conservation laws on unstructured grids. *J Comput Phys* 2011; 230: 7775-7795.
- [36] Li W, Ren YX. The multi-dimensional limiters for solving hyperbolic conservation laws on unstructured grids II: Extension to high order finite volume schemes. *J Comput Phys* 2012; 231: 4053-4077.
- [37] Jiang GS, Shu CW. Efficient implementation of weighted ENO schemes. *J Comput Phys* 1996; 130: 202-228.
- [38] Hu CQ, Shu CW. Weighted essentially non-oscillatory schemes on triangular meshes. *J Comput Phys* 1999; 150: 97-127.
- [39] Krivodonova L, Berger M. High order accurate implementation of solid wall boundary conditions in curved geometries. *J Comput Phys* 2006; 211: 492-512.
- [40] Nejat A, Ollivier-Gooch C. A high order accurate unstructured finite volume Newton–Krylov algorithm for inviscid compressible flows. *J Comput Phys* 2008; 227: 2582–2609.